Materials Characterization 166 (2020) 110440

Contents lists available at ScienceDirect

Materials Characterization

journal homepage: www.elsevier.com/locate/matchar

Defect analysis and 2D/3D-EBSD investigation of an electron beam melted Ti-6Al-4V alloy

Jiang Ma[a], Jinsen Tian[a], Ming Yan[b], Zhuo Chen[c], Jun Shen[a,*], Jing Wu[d,*]

[a] College of Mechatronics and Control Engineering, Shenzhen University, Shenzhen 518060, China
[b] Department of Materials Science and Engineering, Shenzhen Key Laboratory for Additive Manufacturing of High-performance Materials, Southern University of Science and Technology, Shenzhen 518055, China
[c] Aerospace Hiwing (Harbin) Titanium Industrial Co., Ltd., Harbin 150028, China
[d] SUSTech Cryo-EM Center, Southern University of Science and Technology, Shenzhen 518055, China

ARTICLE INFO

Keywords:
Electron beam melting (EBM)
Ti-6Al-4V
3D-EBSD
TEM
Dislocation structure
α variant

ABSTRACT

A Ti-6Al-4V alloy was fabricated by electron beam melting and was characterized by scanning electron microscope (SEM), 2-dimensional/3-dimensional electron backscattered diffraction (2D/3D-EBSD) and transmission electron microscope (TEM). The as-fabricated alloy shows a typical basketweave structure with thin α variants and residual β phase due to the high cooling rate. Six to seven variants are present inside a single β parent grain and each one of the {011} β planes are preferably occupied by only one α variant. The 3D-EBSD result shows detailed 3D configuration of individual α variants, various types of the α/α boundaries and the interaction between these variants. The dislocations formed during the cooling process are mainly ⟨a⟩ type, including the regularly spaced dislocations located near the interface boundary of α/β phase. These detailed microstructure and defect analysis provide fundamental information for tuning the mechanical properties of EBM processed Ti64 alloys.

1. Introduction

Electron beam melting (EBM), as one of the powder bed additive manufacturing techniques, has shown great promises in fabricating Ti64 alloy [1–14]. EBM utilizes electron beam as heating source, which is a rapid solidification process typically resulting in fine structure and the alloy has the potentiality to be both strong and ductile. For example, Galarraga et al. [2] reported an EBM fabricated Ti64 alloy which has a higher ultimate tensile strength compared with the equiaxed α + β structure of conventionally processed wrought materials. But EBM itself is a complicated thermal process and may induce defects like pores and high stress which is harmful for the fatigue properties and ductility. Towards its pathway to commercial applications, lots of efforts have been paid to optimize the mechanical properties, e.g. modifying the EBM processing parameters and introducing post processing techniques such as hot isotropic pressing (HIP) [4,7,8,13–15].

Previous studies on the microstructure were mainly focused on the overall structure and texture evolution to establish a relationship between processing–microstructure–property. Murr et al. [8] reported an EBM-fabricated Ti64 typically has a Widmanstätten or basketweave structure where fine α plates are transformed from high-temperature β matrix during cooling. De Formanoir et al. [4] analyzed the texture of the EBM Ti64 sample using EBSD and revealed a strong ⟨001⟩ pole of the reconstructed high temperature β phase in the build direction. However, due to the complex thermal history of the EBM process, the detailed microstructure, i.e. three-dimensional (3D) morphology and the dislocation structure, which is still lack, maybe significantly different from that of conventional Ti64 alloy.

The 3D morphology is important for understanding the variant selection upon cooling and strain heterogeneities during deformation [16]. Despite its importance, limited studies have been carried out on the α/β titanium alloy, letting alone the EBM processed Ti64. Barriobero-Vila et al. [17] employed X-ray microtomography to study the selective laser melted Ti64 and reported the interconnected β network. However, in order to achieve sub-micron resolution, a synchrotron beam line is necessary, which is not accessible on a laboratory scale [16,17]. Manual serial sectioning combined with optical microscope and EBSD analysis also serves as a strong tool, e.g. a primary α phase is

* Corresponding authors.
E-mail addresses: junshen@szu.edu.cn (J. Shen), wujinguob@163.com (J. Wu).

https://doi.org/10.1016/j.matchar.2020.110440
Received 31 March 2020; Received in revised form 24 May 2020; Accepted 5 June 2020
Available online 10 June 2020
1044-5803/

reconstructed in [18], but it is time consuming and the resolution in Z direction is limited. Recent years, a combination of serial sectioning using focus ion beam (FIB) and EBSD-based orientation microscopy allows fully automatic 3D-EBSD collection with sub-micron resolution in Z axis routinely achievable [19]. S. Hémery et al. [20] employed the 3D-EBSD data as an input for crystal plasticity simulation to access the α-grains in micro-texture regions and shows great promise to predict the mechanical behaviour of Ti64 alloy. In this work, 3D-EBSD will be carried out on the EBM processed Ti64 to study the α variants selection and the interconnection morphology.

The second aim of this work is to assess the dislocation structure in the EBM processed alloy. High residual stress is frequently reported in the additive manufactured alloys and is detrimental to the ductility and fatigue properties [1,21]. The residual stress measured by neutron only provides orientation variation contributed by geometrically necessary dislocations. The analysis of the dislocation structure will be assessed by TEM in detail.

2. Experimental

The Ti64 alloys were fabricated using Acram EBM Q20 machine and the following parameters were used: the layer thickness is 90 μm, speed function is 24, the pre-heat temperature is 700 °C and the vacuum is under 8×10^{-4} Pa. The overall microstructure of as-fabricated alloys was then studied using Tescan Mira-3 SEM and the 2D-EBSD of the XY and YZ sections were scanned using Oxford Instruments EBSD detector. The scan areas of the XY and YZ sections are of 365 × 294 μm and 343 × 257 μm respectively, and the step size is 0.3 μm. The 2D-EBSD data was processed using Atex software [22].

The 3D-EBSD analysis was carried out using an FEI G4 Xe plasma FIB equipped with Bruker e-flash detector, ASV (AutoSlice&View) software, automatic stage movement and EBSD collection. The 3D-EBSD is reconstructed from an aligned stack of the 2D-EBSD slices. Unlike gray scale SEM images, every stack has crystallographic information and forms a 4D databank. This involves a repeated process where a thin slice of material is removed using ion beam, thus a fresh surface is exposed for a 2D-EBSD to be collected. The slice thickness is 150 nm, and the step size of the EBSD scan is approximately 100 nm. In order to maximise the EBSD signal, a chunk of as-fabricated alloy with size of about 23 × 23 × 29 μm was lift out using AutoLift and welded onto the edge of a silicon wafer so that no obstacles are on the way to block EBSD signal to EBSD detector. To reduce the curtaining effect, which is more predominant in plasma-FIB than Ga-FIB, the liftout chunk is protected by Pt coating and 'rock milling' is applied by appropriate stage movement and scanning beam rotation to provide two tilted milling direction. After data collection, the 2D-EBSD data were imported into Qube software. After aligning the stacks, 3D data was reconstructed and denoised. Individual α variant can be singled out based on its Euler angle extracted from the pole figure.

Two-beam conditions were used to determine the Burgers vectors of the dislocations. The TEM related analysis were carried out using FEI Talos F200 equipped with super-X EDS detector and the sample was prepared using Struers tenupol-5 twin-jet electropolishing using 50 mL $HClO_4$, 350 mL butanol and 600 mL methanol.

3. Results

3.1. Overall microstructure of the as-fabricated sample

Fig. 1 shows a typical XY section and a YZ section of the as-fabricated Ti64 sample. Both sections appear to be similar in morphology under the same magnification. The majority phase is α plate and the thin plates with brighter contrast are residual β phase from high temperature, which results in a typical basketweave.

Fig. 2a and b show the STEM bright-field image and the EDS mapping of the same region, where more V and less Al are observed in the thin β phase. Quantification of the point analysis indicates that the chemical compositions of the α and β phases are $Ti_{90.3 \pm 0.2}Al_{9.0 \pm 0.2}V_{0.7 \pm 0.1}$ (at.%) and $Ti_{78.8 \pm 3.4}Al_{4.1 \pm 1.1}V_{17.1 \pm 4.4}$ (at.%), respectively. This process is diffusional transformation in contrast to the diffusionless martensite transformation in some EBM processes [23]. Fig. 2c shows a needle-shaped β phase and the surrounding α phase at higher magnifications. The corresponding diffraction pattern (displayed in Fig. 2d) confirms that the [0001] zone axis of the α phase is parallel to the [011] zone axis of the β phase. Hence, the Burgers orientation relationship is still valid between α and β phases in the EBM process.

3.2. 2D-EBSD results of the XY and YZ sections of as-fabricated alloy

Figs. 3 and 4 compare the orientation maps of the XY section and YZ section with relatively large EBSD scan area to show the parent β grain

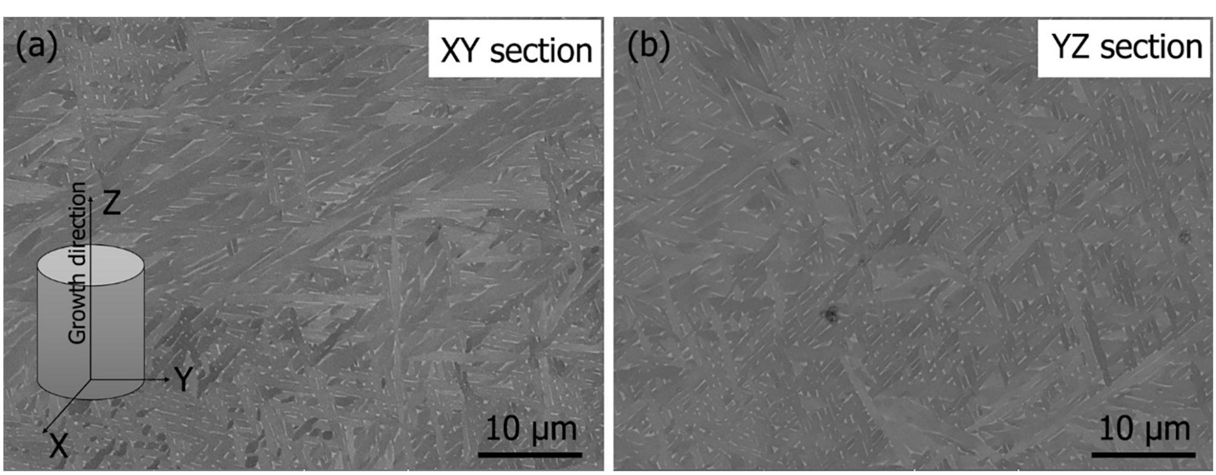

Fig. 1. BSE images showing the structure of EBM-fabricated Ti64 alloy; inserted is the schematic drawing of the sample section: (a) XY section; (b) YZ section.

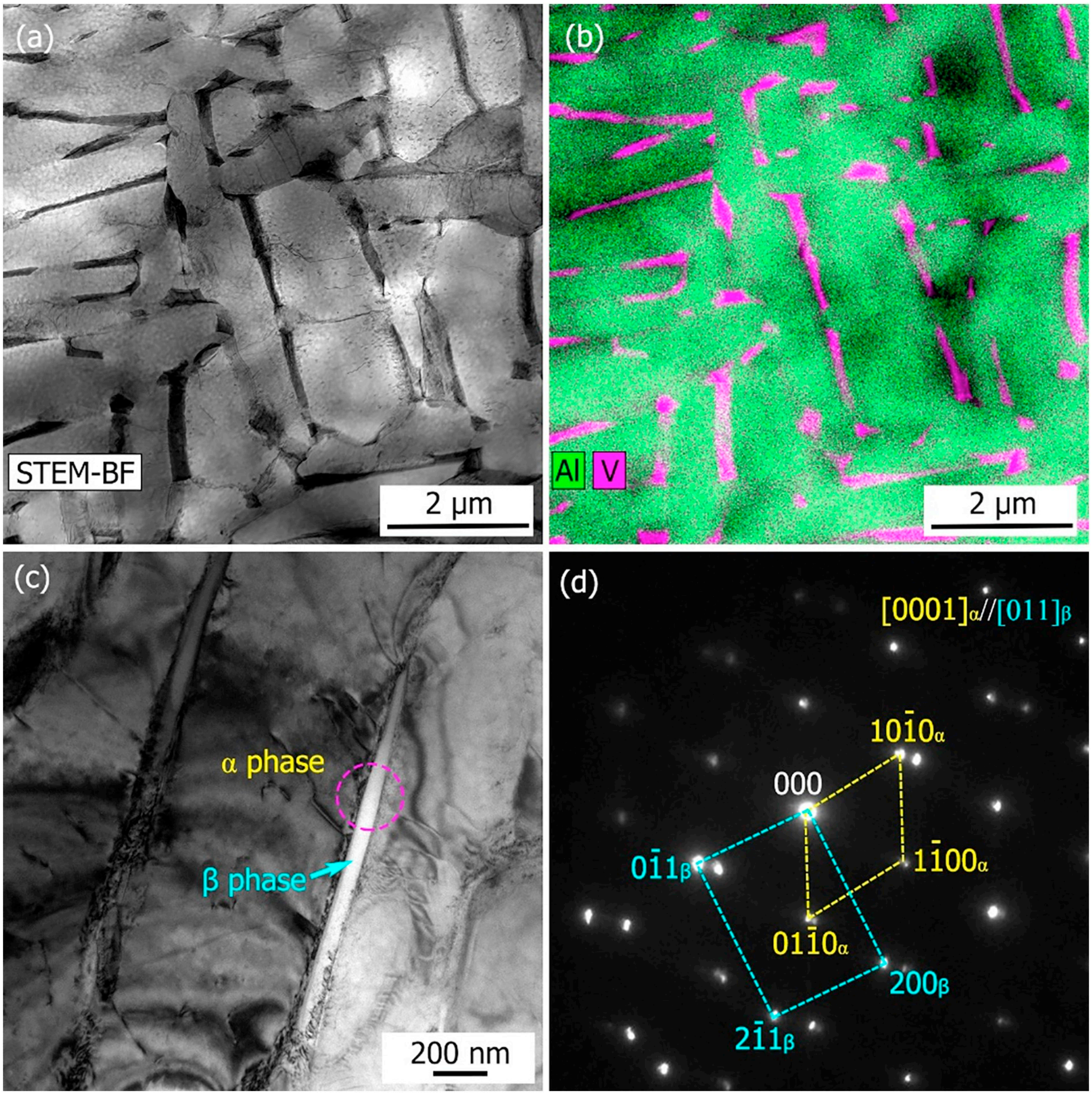

Fig. 2. (a) STEM bright-field image and (b) EDS mapping of the same region indicates that the β phase is rich in V and depleted in Al. (c) TEM bright field image showing the α and β phases; (d) The diffraction pattern of the α and β phases corresponding to the circular dashed region in Figure c indicates the following orientation relationship: $[0001]_{\alpha}$ / / $[011]_{\beta}$.

and the overall structure of as fabricated Ti64 alloy. Despite α plates possess different orientations in XY section, they appear to have patterns over a region typically larger than 200 μm (e.g. the labeled regions ①–⑦). The normal direction of these β grains can be reconstructed accordingly by Burgers relationship and the results are summarized in the inserted inverse pole figure. Fig. 4 shows the YZ section has different morphology compared with XY section, the left half part is likely from the same parent β grain. Although only part of the grain is captured, it is reasonable to assume the grains are likely to be an elongated form with its longer side along growth direction.

3.3. 3D characterization of the α variants

3D-EBSD was used to investigate the α variant configurations inside the parent β grain. Fig. 5a illustrates the stacking of thin-layered EBSD results, and post-processing software was applied to reconstruct the 3D volume and obtain the orientation information in the z direction (building direction). The series of 2D-EBSD results were obtained automatically using FIB-SEM, where EBSD scanning occurred repeatedly after a certain thickness of materials was removed using the ion beam. The reconstructed 3D volume view and the orthogonal slice view of α

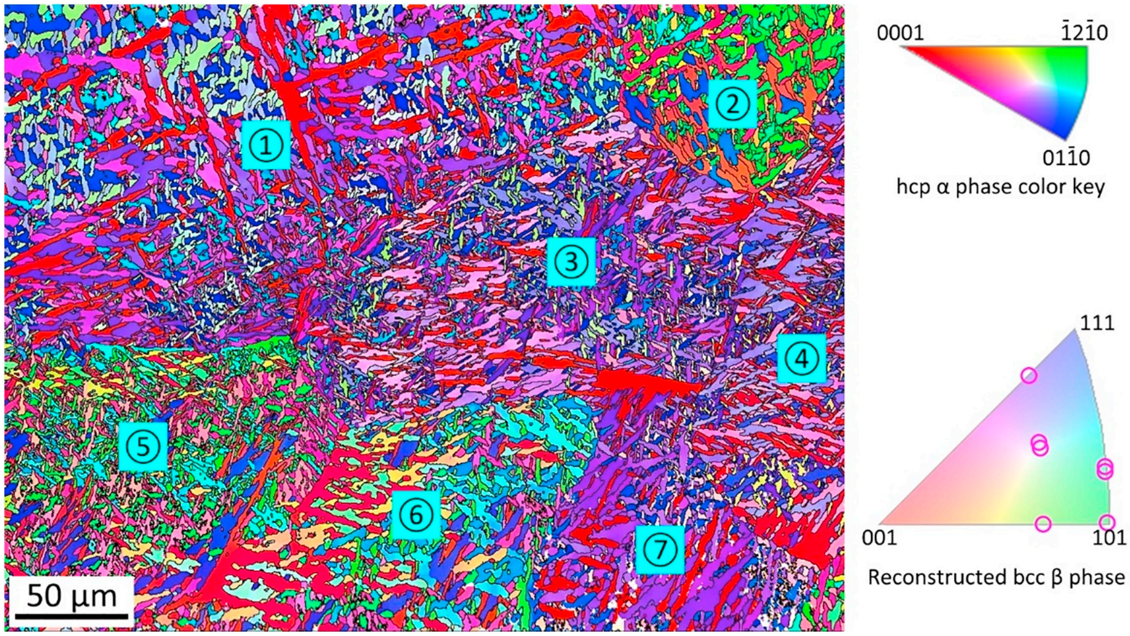

Fig. 3. 2D-EBSD IPFz map of the XY section of the Ti64 alloy. The small circles in inverse pole figure in the lower right corner shows the normal directions of the parent β grains.

variants are presented in Fig. 5b and c. The size of the whole volume is 23 μm × 23 μm × 29 μm (building direction), and the different colors represent different α variants. The α variant shows a lense shaped view from x, y, and z directions (Fig. 5c); hence, this variant has a plate shape with edge thinner than the middle part. This finding was confirmed by the individual variant morphologies shown in Fig. 6, which also indicates that the shape of the plate is irregular. Fig. 5d shows the {0001} pole figure of the α variants, and six maxima (of the black spots) can be observed. Each maxima corresponds to one or two α variants; thus, at least six variants can be found in this region. These maxima also correspond to the six {011} planes of a β phase, thereby confirming the Burgers orientation relationship: $\{0001\}_{\alpha}//\{011\}_{\beta}$. The

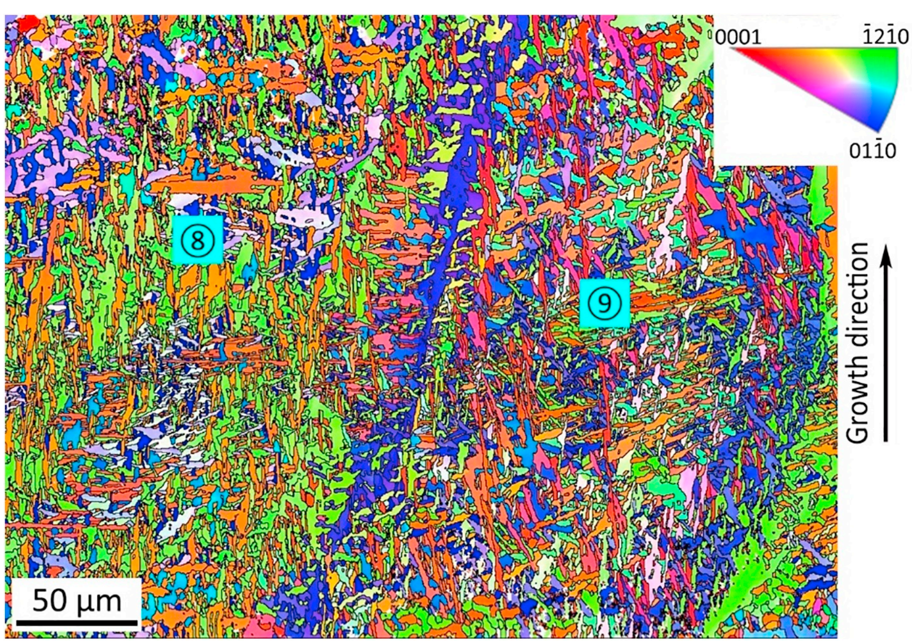

Fig. 4. The IPFz map of the YZ section shows the grain may be in an elongated form.

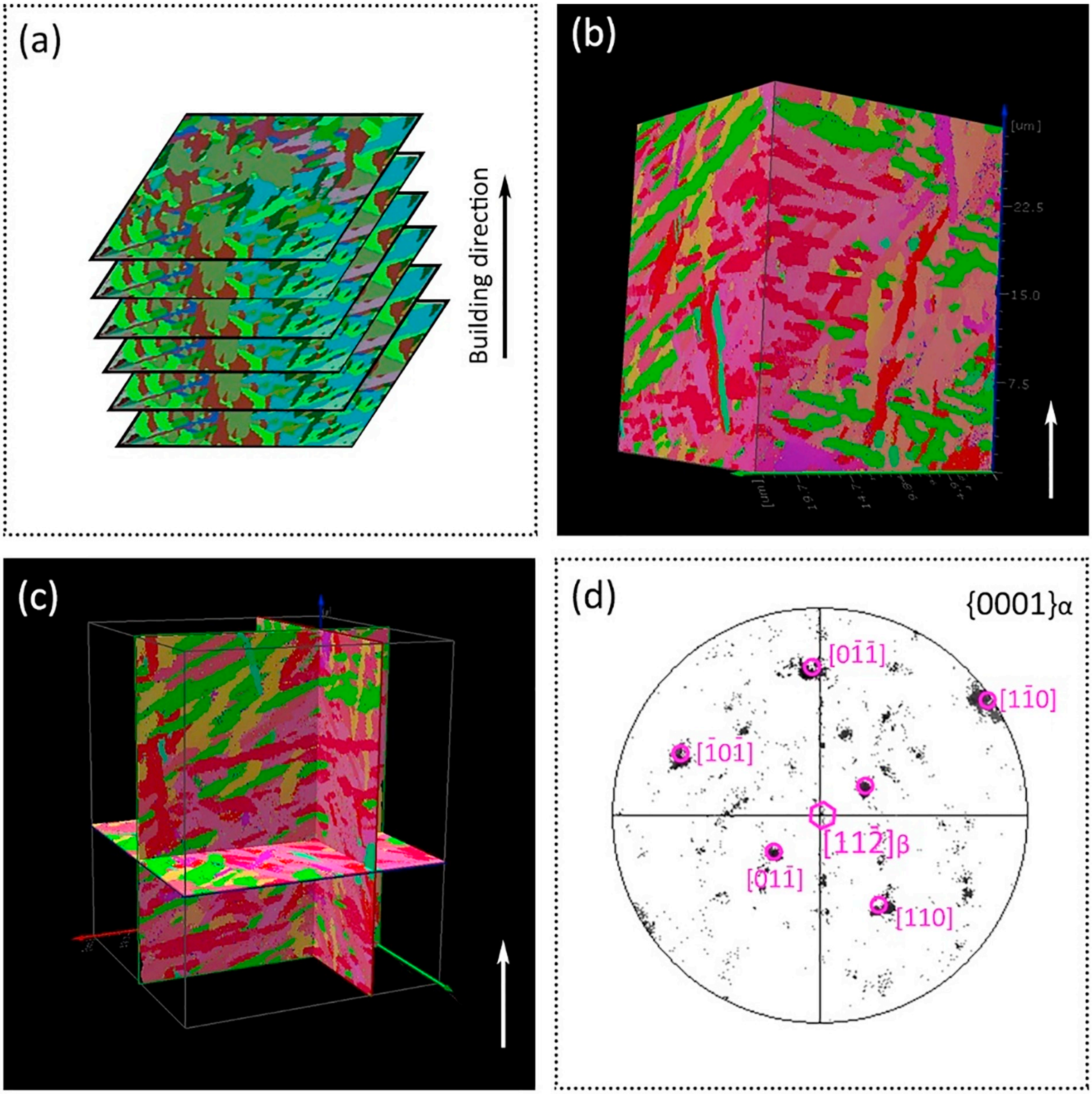

Fig. 5. (a) Schematic image of the principle of 3D-EBSD; (b) Reconstructed α variants in 3D volume showing the overall structure; (c) Orthogonal slice view showing the morphology of the α variants in three directions; (d) Pole figure of the {0001} planes showing the α variants in black spots and the reconstructed ⟨110⟩ zone axis of parent β phase (indicated by magenta circles) based on Burgers transformation, indicating that the building direction of this particular parent β phase is [$11\bar{2}$] zone axis. (For interpretation of the references to colour in this figure legend, the reader is referred to the web version of this article.)

zone axis of the parent β grain along the building direction is identified as [$11\bar{2}$].

Fig. 6 shows the morphologies of the eight α variants in this region, which is labeled as V1-V8. The orientation relationship between V1-V8 and parent β phase are listed in Table 1. The α precipitates from the same variant are all aligned on the same plane, assuming to be the broad face $(\bar{1}\bar{1}\ 13\ 11)_\beta$. The high cooling rate of the EBM process induced obvious local orientation variation (gradual colour change) in α plates. This is more obvious in Fig. 6b.

3.4. The dislocation structure of the as-fabricated sample in TEM

Two-beam conditions are used to analyse the Burgers vector types of the dislocations in Ti64 alloy. Fig. 7a shows a dislocation network appears in hexagonal shape in the middle grain under the beam condition g = $01\bar{1}\bar{1}$ and these dislocations were out of contrast when the g vector is 0002 (Fig. 7b). This suggests these dislocations were ⟨a⟩ type dislocations and probably have two or more ⟨a⟩ type Burgers vectors to form a dislocation network. Fig. 7c and d are STEM HAADF images

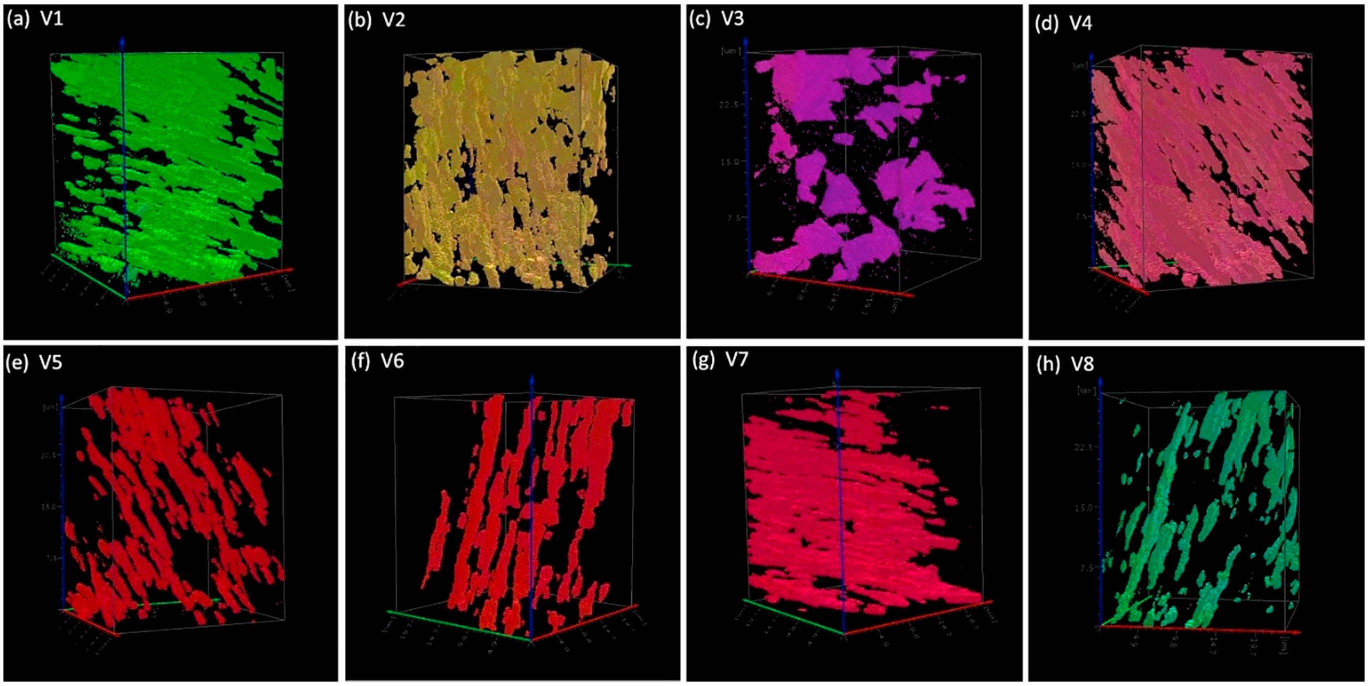

Fig. 6. Individual α variant distributions of the as-fabricated sample.

Table 1
Types of grain boundaries formed between adjacent α variants V1-V8. The definition of the different types is presented by Wang. et al. [26].

	Orientation relationship	V1	V2	V3	V4	V5	V6	V7	V8
V1	$(1\bar{1}0)_\beta//(0001)_\alpha$, $[111]_\beta//[11\bar{2}0]_\alpha$	1	2	5	2	3	3	4	6
V2	$(10\bar{1})_\beta//(0001)_\alpha$, $[111]_\beta//[11\bar{2}0]_\alpha$	2	1	4	2	5	4	3	3
V3	$(110)_\beta//(0001)_\alpha$, $[\bar{1}11]_\beta//[11\bar{2}0]_\alpha$	5	4	1	3	3	4	3	5
V4	$(01\bar{1})_\beta//(0001)_\alpha$, $[111]_\beta//[11\bar{2}0]_\alpha$	2	2	3	1	4	5	5	3
V5	$(101)_\beta//(0001)_\alpha$, $[11\bar{1}]_\beta//[11\bar{2}0]_\alpha$	3	5	3	4	1	2	3	2
V6	$(011)_\beta//(0001)_\alpha$, $[11\bar{1}]_\beta//[11\bar{2}0]_\alpha$	3	4	4	5	2	1	6	2
V7	$(011)_\beta//(0001)_\alpha$, $[1\bar{1}1]_\beta//[11\bar{2}0]_\alpha$	4	3	3	5	3	6	1	3
V8	$(1\bar{1}0)_\beta//(0001)_\alpha$, $[11\bar{1}]_\beta//[11\bar{2}0]_\alpha$	6	3	5	3	2	2	3	1

showing a common phenomenon where lots of organised dislocation present in the vicinity of α/β boundary, as indicated by the red arrows. These dislocations are analyzed in detail in Fig. 8. Fig. 8a shows a region with aligned β phase from the same colony. The magnified image Fig. 8b indicates the well organised dislocations appears on the top surface of the β phase, and they lose contrast when g = 0002 (Fig. 8c) which confirms the identity of these dislocations are also ⟨a⟩ type. Besides ⟨a⟩ dislocations, ⟨c + a⟩ dislocations are also observed in Fig. 8c. They are visible under g = 0002 and g = $\bar{2}110$. It is interesting to notice that many ⟨c + a⟩ dislocations consist of straight components and some components are parallel to the basal plane as arrowed in Fig. 8c.

4. Discussion

4.1. Variant selection of EBM processed Ti64

The hcp structure of α phase is highly anisotropic compared with cubic β phase. During β transformation, α and β phases maintain the Burgers orientation relationship, and theoretically, 12 equivalent α variants are presented within a single prior β grain [24]. However, some α variants appear more frequently than the others [25,26]. Simonelli et al. [25] reported that in Ti64 alloy fabricated by selective laser melting, all 12 variants exist, but only 6 are the preferred orientations. Our results show similar trend, as summarized in Fig. 9, typically 6–7 variants are dominant in a parent β grain. The overall area fraction of 6 variants exceeded 85%. The 6 variants are likely to share different {110} planes in parent grain indicated by the pole figures, which is not shown here. Due to the possibility of 12 equivalent α variants co-exist in a single β grain and consequently, six types of α/α boundaries appear depending on the reduced axis/angle pairs [26]. Fig. 10 shows the misorientation angles between α variants and indicates 3 peaks around 10°, 60° and 90°. The peak around 10° corresponds to [0001]/10.53° rotation axis/rotation angle pair, it shows the lowest relative frequency which also confirms that only one preferred α variant precipitates along the {110} planes in parent β grains. There is need to point out that the area fractions of α variant in larger area in 2D-EBSD may be representative of the true volume fraction if the parent β are randomly oriented. However, area fraction is based on the 2D projection of the α variant, if the α plates were parallel or incline to the EBSD scanning surface, it may contribute more to the area fraction

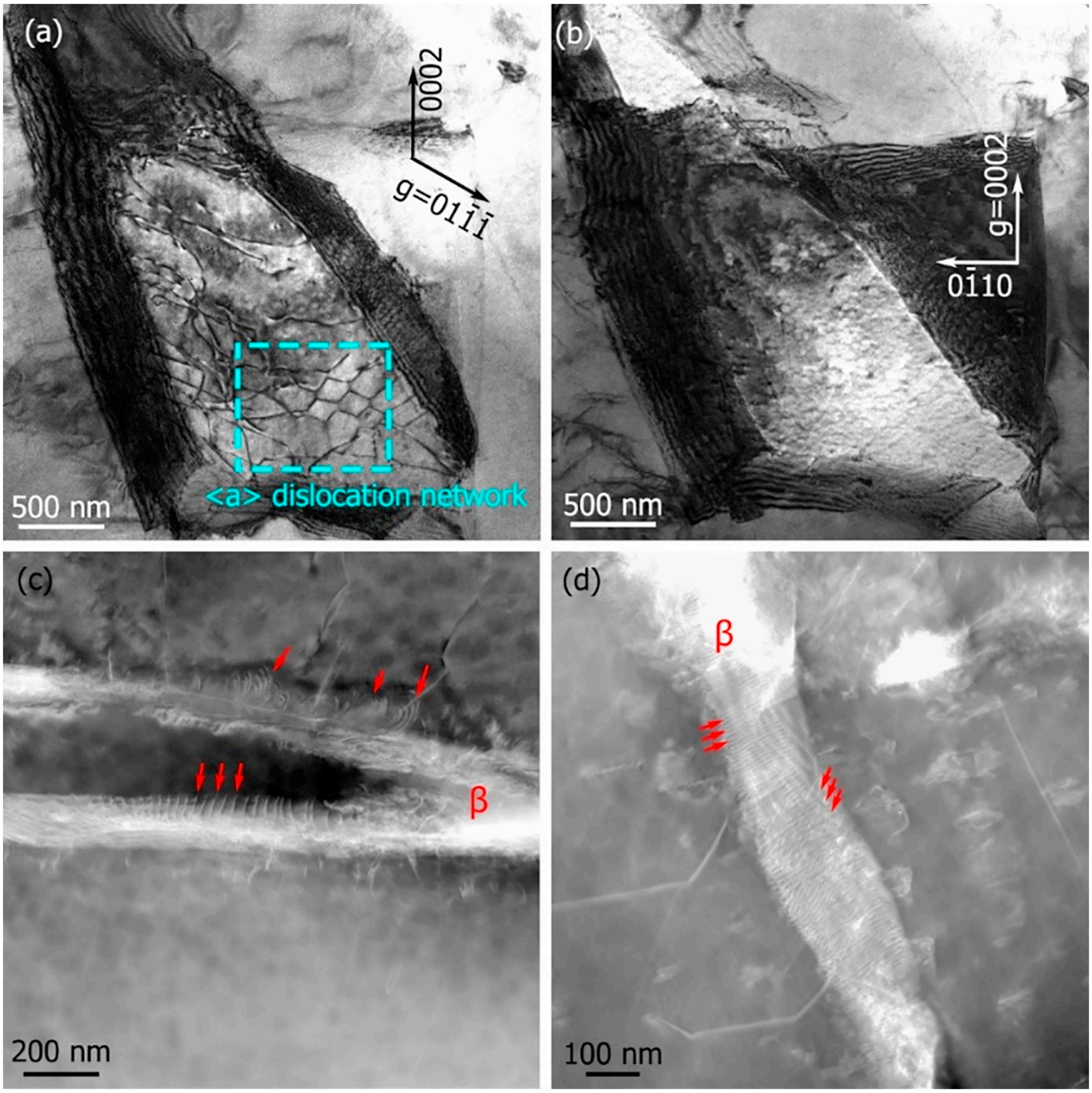

Fig. 7. (a) (b) TEM bright field images of the same α grain under different two beam conditions showing an ⟨a⟩ type dislocation network; (c) and (d) STEM HAADF images showing lots of dislocations indicated by arrows were observed around β phase.

measurement. That is the case for EBM processed Ti64 with a dominant texture.

Compared with 2D-EBSD, 3D-EBSD can only image relatively small volume, but more details are revealed. Fig. 6 reveals the 3D morphology of the variants that were thin plates with irregular shape, and the orientation of each variantis parallel to each other. Furthermore, the interaction between each variant was also of significance. Fig. 9 presents a few examples of interaction between different α variants. Without the information of the growth sequence, the red variant in Fig. 9a appears to attempt to grow around the yellow variant, eventually forming an α/α boundary. Table 1 lists all types of α/α pairs in this region, according to the definition by Wang et al. [26]. For example, V1 and V2 share a type 2 ([11$\bar{2}$0]/60°) boundary, which indicates that [11$\bar{2}$0] is the common axis parallel to $[111]_\beta$ zone axis of the parent β phase and the misorientation angle is 60°. Fig. 9b shows the two differently oriented α variants (V3 and V4) relatively spaced in the 3D volume and connected to each other to form a skeleton. The boundary between V3/V4 belongs to type 3, where the common axis is [$\bar{1}\bar{0}$ $\bar{7}$ 17 3], and the rotation angle is approximately 60.83°. Fig. 9c and d present the evidence of the interconnection between V1 and V8, with one variant goes around another or goes through it. The result indicates that all the possibilities exist. For example, in relation to V8 grain (Fig. 9d),

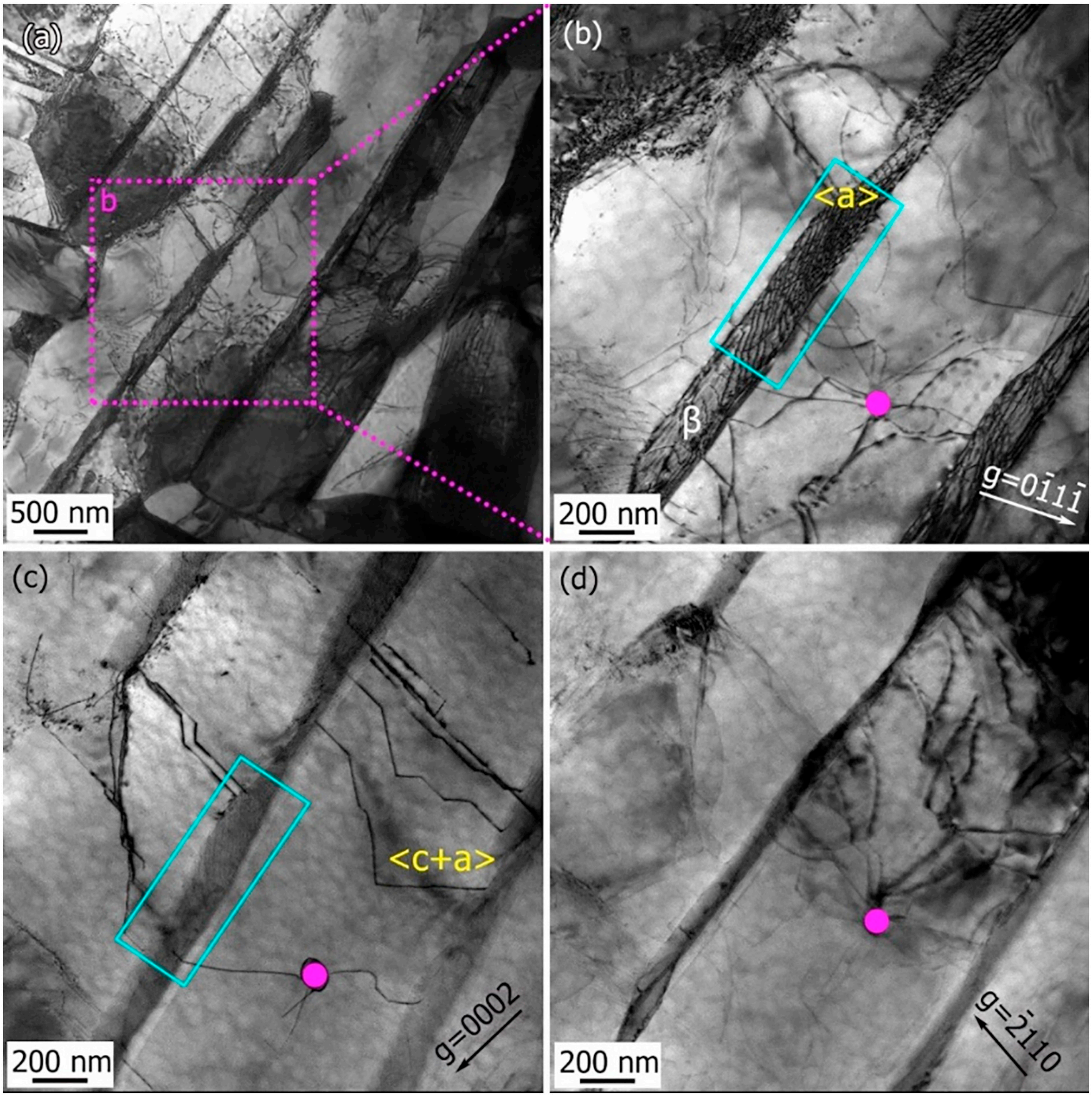

Fig. 8. TEM bright field images with two beam conditions showing the dislocations has ⟨a⟩ type and ⟨c + a⟩ type. Fig. 8a shows a typical area containing few α laths in the middle which belong to the same variant. Fig. 8b–d shows detailed dislocation structure using two beam conditions with different g vectors. A magenta spot is labeled at the same position to guide the eyes. (For interpretation of the references to colour in this figure legend, the reader is referred to the web version of this article.)

V1-a, V1-b, and V1-c grains show three cases: V1-a went through V8 grain (in other words, V8 surrounds V1-a); V1-b stopped at the interface; and V8 stopped at V1-c. This finding suggests that no obvious precipitation sequence occurred between V1 and V8. Lee et al. [27] reported that the coupling between α variants in basketweave structure are not random and may be selected by certain criteria. Shi et al. [28] investigated the variant selection under the influence of internal and external stresses and suggested that the interplay between external stress or strain and internal stress generated by the precipitation itself determines the variant selection.

Additive manufactured Ti64 is generally a textured material due to the temperature gradient along the building direction, and this can lead to anisotropic mechanical behaviors [13,29]. It is difficult to establish the direct link between the texture variation and mechanical properties due to the β to α transformation and variant selection process. Although the parent β grain possesses a dominant growth direction along ⟨001⟩ zone axis [9,14], the resulting structure is fine grained α variants. Since 3D-EBSD can help understanding the morphology and orientation of the

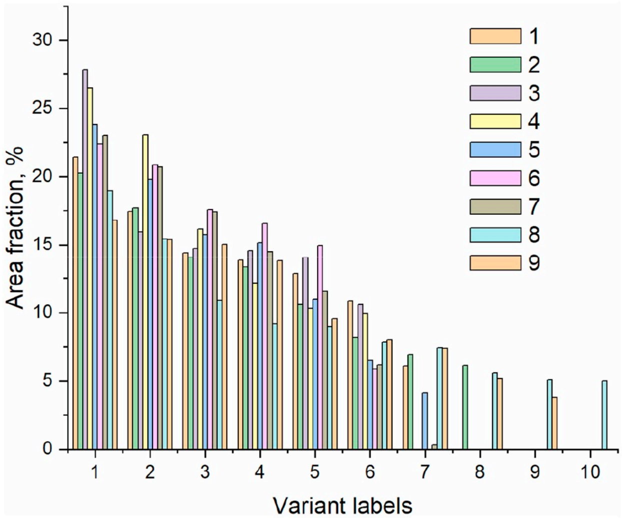

Fig. 9. The area fractions of α variants summarized from seven grains in Figs. 3 and 2 grains in Fig. 4. The α variants are labeled in decedent order of area fractions.

α variants, it is possible to use this information for crystal plasticity modelling input to predict the mechanical behaviour of the α variants inside individual β grain. The crystal plasticity and the experimental validation will be part of a future work (Fig. 11).

4.2. Dislocation structure of EBM processed Ti64

Due to the high cooling rate of the EBM process, high residual stress was frequently observed using X-ray, however, X-ray can only reveal the geometrically necessary dislocations which contribute to the orientation variation. This TEM work visualize both geometrically necessary dislocations and others which don't contribute to the orientation variation. The as-fabricated alloy has a high density of dislocations, which agrees with observation from literatures [8,30]. Our detailed Burgers vector analysis reveals that dislocations generated during the fabrication process are mainly ⟨a⟩ type. This includes randomly distributed dislocations, well organised dislocation network and regularly spaced dislocations in the α/β interface (Figs. 7 and 8). The ⟨c + a⟩ dislocations are occasionally observed (Fig. 8c,d). ⟨a⟩ dislocations are dominant dislocations in Ti64 during deformation, which have significantly lower critical resolved shear stress (CRSS) compared with ⟨c + a⟩ dislocations. Most of the ⟨a⟩ type dislocations are mobile and can easily move when applying appropriate stress. However, given the Burgers orientation relationship between α/β phase, different ⟨a⟩ type dislocations exhibit different behaviors [31]. The dislocation with $a_1 = 1/3[2\bar{1}\bar{1}0]$ Burgers vector on prismatic plane can transmit through an α/β boundary to β phase as corresponding slip system or vice versa, while dislocations with Burgers vector of $a_2 = 1/3[1\bar{2}10]$ or $a_3 = 1/3[11\bar{2}0]$ do not easily transmit through and eventually pile up at the interface boundary. These dislocation pileups at interfaces can further facilitate more dislocation emissions.

Residual β phase and α/β interface are potential dislocations nucleation sites in the alloy. Fig. 7c indicates the dislocations bows out from either the β phase or the interface and moves into the α interface. The β phase is generally softer than α phase and lower thermal stress is needed to active slip systems. It is interesting to notice that the regularly spaced dislocations close to the α/β interfaces are ⟨a⟩ type. Due to the semi-coherency of the α and the β, the interface generally has a broad face (i.e. $(\bar{1}\bar{1}\ 13\ 1)_\beta$) which contains ⟨c⟩ misfit dislocations, a side face and an edge phase which contains ⟨a⟩ misfit dislocations [31]. It seems contradictory that the dislocations observed close to the broad face of α/β interface in Fig. 8 belong to ⟨a⟩ type. This may be explained by different expansion rate between α and β phase causing misfit during the rapid cooling process. So dislocation maybe formed near α/β interface. This also indicates the α/β interface is potential dislocation nucleation sites.

5. Conclusion

Multi-scale microstructure analysis of EBM fabricated Ti64 alloy is carried out using combination of 2D-EBSD, 3D-EBSD and TEM. The as-fabricated alloy contains a basketweave structure, where α and β phases maintain the Burgers orientation relationship. Typically six to seven variants were present inside a single β parent grain and each one of the {011} planes of β grain is occupied by typically one variant. The 3D-EBSD analysis indicates that an individual α variant has a plate shape with an edge thinner than the middle part and aligned parallel to each other. The α plates from different variants formed a skeleton structure, and different types of α/α boundaries are viewed. The TEM work revealed that the dominant dislocation type in as-fabricated Ti64 alloys was ⟨a⟩ type, including the regularly spaced dislocations close to the α/β interface.

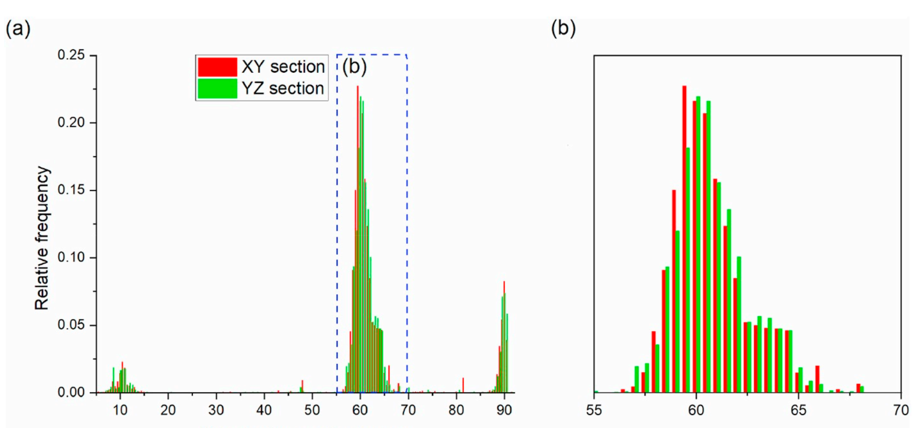

Fig. 10. The relative frequency of misorientation angles between α variants: (a) overall view; (b) the magnified area indicated by dashed rectangle in (a).

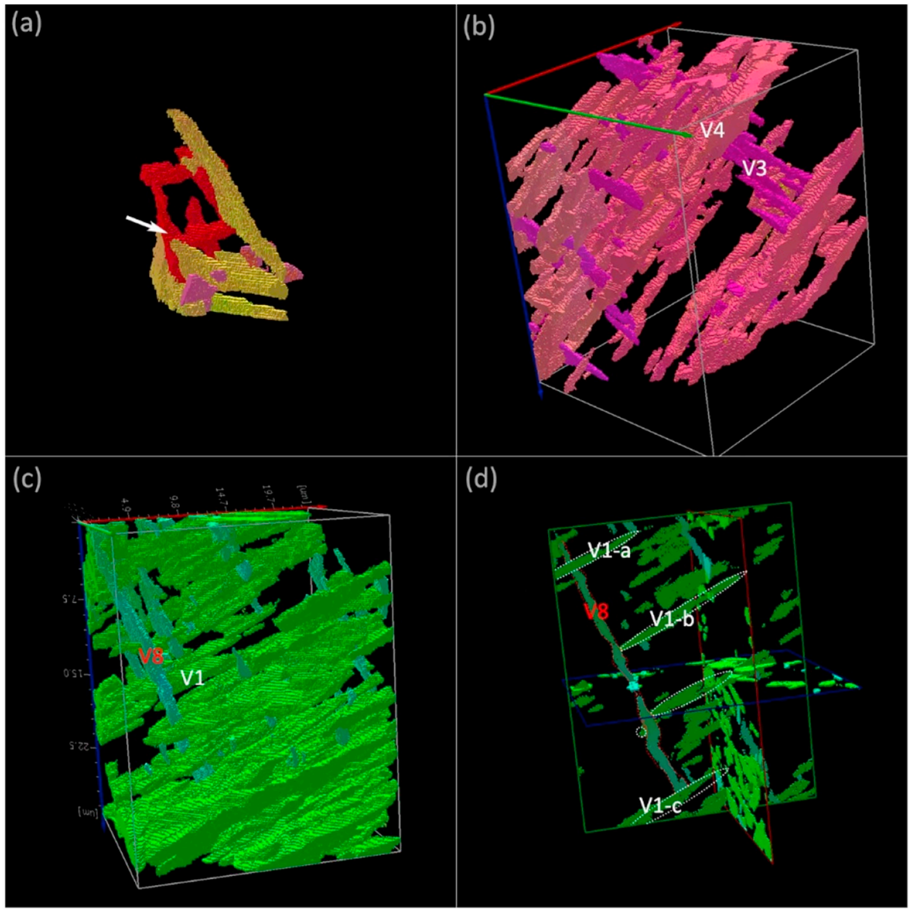

Fig. 11. (a) Few neighboring α variants separated by different colors; (b) morphology of α grains that belong to two attached variants; (c) (d) 3D volume and orthogonal slices showing the growth of the two variants.

Data availability

The raw/processed data required to reproduce these findings cannot be shared at this time due to technical or time limitations.

Declaration of competing interest

The authors declare that they have no known competing financial interests or personal relationships that could have appeared to influence the work reported in this paper.

Acknowledgment

This research did not receive any specific grant from funding agencies in the public, commercial, or not-for-profit sectors.

References

[1] N. Hrabe, T. Gnäupel-Herold, T. Quinn, Fatigue properties of a titanium alloy (Ti–6Al–4V) fabricated via electron beam melting (EBM): effects of internal defects and residual stress, Int. J. Fatigue 94 (2017) 202–210.
[2] H. Galarraga, R.J. Warren, D.A. Lados, R.R. Dehoff, M.M. Kirka, P. Nandwana, Effects of heat treatments on microstructure and properties of Ti-6Al-4V ELI alloy fabricated by electron beam melting (EBM), Mater. Sci. Eng. A 685 (2017) 417–428.
[3] A. Safdar, L.Y. Wei, A. Snis, Z. Lai, Evaluation of microstructural development in electron beam melted Ti-6Al-4V, Mater. Charact. 65 (2012) 8–15.
[4] C. de Formanoir, S. Michotte, O. Rigo, L. Germain, S. Godet, Electron beam melted Ti–6Al–4V: microstructure, texture and mechanical behavior of the as-built and heat-treated material, Mater. Sci. Eng. A 652 (2016) 105–119.
[5] C. Wei, X. Ma, X. Yang, M. Zhou, C. Wang, Y. Zheng, W. Zhang, Z. Li, Microstructural and property evolution of Ti6Al4V powders with the number of usage in additive manufacturing by electron beam melting, Mater. Lett. 221 (2018) 111–114.
[6] J. Karlsson, A. Snis, H. Engqvist, J. Lausmaa, Characterization and comparison of materials produced by Electron beam melting (EBM) of two different Ti–6Al–4V powder fractions, J. Mater. Process. Technol. 213 (2013) 2109–2118.
[7] N. Hrabe, T. Quinn, Effects of processing on microstructure and mechanical properties of a titanium alloy (Ti–6Al–4V) fabricated using electron beam melting (EBM), part 1: distance from build plate and part size, Mater. Sci. Eng. A 573 (2013) 264–270.
[8] L.E. Murr, E.V. Esquivel, S.A. Quinones, S.M. Gaytan, M.I. Lopez, E.Y. Martinez, F. Medina, D.H. Hernandez, E. Martinez, J.L. Martinez, S.W. Stafford, D.K. Brown, T. Hoppe, W. Meyers, U. Lindhe, R.B. Wicker, Microstructures and mechanical properties of electron beam-rapid manufactured Ti–6Al–4V biomedical prototypes compared to wrought Ti–6Al–4V, Mater. Charact. 60 (2009) 96–105.
[9] S.S. Al-Bermani, M.L. Blackmore, W. Zhang, I. Todd, The origin of microstructural diversity, texture, and mechanical properties in electron beam melted Ti-6Al-4V, Metall. Mater. Trans. A 41 (2010) 3422–3434.
[10] T. Persenot, G. Martin, R. Dendievel, J.-Y. Buffiére, E. Maire, Enhancing the tensile properties of EBM as-built thin parts: effect of HIP and chemical etching, Mater. Charact. 143 (2018) 82–93.
[11] M. Seifi, M. Dahar, R. Aman, O. Harrysson, J. Beuth, J.J. Lewandowski, Evaluation of orientation dependence of fracture toughness and fatigue crack propagation behavior of as-deposited ARCAM EBM Ti-6Al-4V, JOM 67 (2015) 597–607.
[12] A.N. Kalinyuk, N.P. Trigub, V.N. Zamkov, O.M. Ivasishin, P.E. Markovsky, R.V. Teliovich, S.L. Semiatin, Microstructure, texture, and mechanical properties of electron-beam melted Ti–6Al–4V, Mater. Sci. Eng. A 346 (2003) 178–188.
[13] J. Bruno, A. Rochman, G. Cassar, Effect of build orientation of electron beam melting on microstructure and mechanical properties of Ti-6Al-4V, J. Mater. Eng. Perform. 26 (2017) 692–703.
[14] A.A. Antonysamy, J. Meyer, P.B. Prangnell, Effect of build geometry on the β-grain structure and texture in additive manufacture of Ti6Al4V by selective electron beam melting, Mater. Charact. 84 (2013) 153–168.
[15] N. Hrabe, T. Quinn, Effects of processing on microstructure and mechanical properties of a titanium alloy (Ti–6Al–4V) fabricated using electron beam melting (EBM), part 2: energy input, orientation, and location, Mater. Sci. Eng. A 573 (2013) 271–277.
[16] N. Vanderesse, E. Maire, M. Darrieulat, F. Montheillet, M. Moreaud, D. Jeulin, Three-dimensional microtomographic study of Widmanstätten microstructures in an alpha/beta titanium alloy, Scr. Mater. 58 (2008) 512–515.

[17] P. Barriobero-Vila, J. Gussone, J. Haubrich, S. Sandlöbes, J. Da Silva, P. Cloetens, N. Schell, G. Requena, Inducing stable α + β microstructures during selective laser melting of Ti-6Al-4V using intensified intrinsic heat treatments, Materials 10 (2017) 268.
[18] H. Sharma, S.M.C. van Bohemen, R.H. Petrov, J. Sietsma, Three-dimensional analysis of microstructures in titanium, Acta Mater. 58 (2010) 2399–2407.
[19] D. He, S. Zaefferer, J. Zhu, Z. Lai, Three-dimensional Morphological and Crystallographic Investigation of Lamellar Alpha and Retained Beta in a Near Alpha Titanium Alloy by Combination of Focused Ion Beam and Electron Backscattering Diffraction, 83 (2012), pp. 496–500.
[20] S. Hémery, A. Naït-Ali, M. Guéguen, J. Wendorf, A.T. Polonsky, M.P. Echlin, J.C. Stinville, T.M. Pollock, P. Villechaise, A 3D analysis of the onset of slip activity in relation to the degree of micro-texture in Ti–6Al–4V, Acta Mater. 181 (2019) 36–48.
[21] D.D. Gu, W. Meiners, K. Wissenbach, R. Poprawe, Laser additive manufacturing of metallic components: materials, processes and mechanisms, Int. Mater. Rev. 57 (2012) 133–164.
[22] B. Beausir, J.-J. Fundenberger, Analysis Tools for Electron and X-ray Diffraction, ATEX - Software, www.atex-software.eu.
[23] S.L. Lu, M. Qian, H.P. Tang, M. Yan, J. Wang, D.H. StJohn, Massive transformation in Ti–6Al–4V additively manufactured by selective electron beam melting, Acta Mater. 104 (2016) 303–311.
[24] W.G. Burgers, On the process of transition of the cubic-body-centered modification into the hexagonal-close-packed modification of zirconium, Physica 1 (1934) 561–586.
[25] M. Simonelli, Y.Y. Tse, C. Tuck, On the texture formation of selective laser melted Ti-6Al-4V, Metall. Mater. Trans. A 45 (2014) 2863–2872.
[26] S.C. Wang, M. Aindow, M.J. Starink, Effect of self-accommodation on α/α boundary populations in pure titanium, Acta Mater. 51 (2003) 2485–2503.
[27] E. Lee, R. Banerjee, S. Kar, D. Bhattacharyya, H.L. Fraser, Selection of α variants during microstructural evolution in α/β titanium alloys, Philos. Mag. 87 (2007) 3615–3627.
[28] R. Shi, Y. Wang, Variant selection during α precipitation in Ti–6Al–4V under the influence of local stress – a simulation study, Acta Mater. 61 (2013) 6006–6024.
[29] B.E. Carroll, T.A. Palmer, A.M. Beese, Anisotropic tensile behavior of Ti–6Al–4V components fabricated with directed energy deposition additive manufacturing, Acta Mater. 87 (2015) 309–320.
[30] L.E. Murr, S.A. Quinones, S.M. Gaytan, M.I. Lopez, A. Rodela, E.Y. Martinez, D.H. Hernandez, E. Martinez, F. Medina, R.B. Wicker, Microstructure and mechanical behavior of Ti–6Al–4V produced by rapid-layer manufacturing, for biomedical applications, J. Mech. Behav. Biomed. Mater. 2 (2009) 20–32.
[31] S. Suri, G.B. Viswanathan, T. Neeraj, D.H. Hou, M.J. Mills, Room temperature deformation and mechanisms of slip transmission in oriented single-colony crystals of an α/β titanium alloy, Acta Mater. 47 (1999) 1019–1034.